J Mater Sci (2011) 46:7517–7524
DOI 10.1007/s10853-011-5723-1

Electrospinning preparation and photoluminescence properties of $SrAl_2O_4:Ce^{3+}$ nanowires

Ruifang Zheng · Lin Xu · Weifeng Qin · Jiansheng Chen · Biao Dong · Ligong Zhang · Hongwei Song

Received: 7 March 2011 / Accepted: 16 June 2011 / Published online: 25 June 2011

Abstract One-dimensional monoclinic $SrAl_2O_4:Ce^{3+}$ nanowires (NWs) were prepared by the electrospinning method for the first time. By annealing PVP/$SrAl_2O_4:Ce^{3+}$ composite nanowires (NWs) with different ratio of PVP ($M_w \approx 1300000$) to inorganic precursors of the electrospinning solutions, size-controllable NWs were obtained, ranging of 90–180 nm. Fourier transform infrared spectroscopy (FTIR), X-ray powder diffraction (XRD), scanning electron microscopy (SEM), photoluminescence (PL) spectra, and dynamics were employed to characterize the NWs. The results demonstrate that the positions of excitation and emission bands varied uneven with the ratio of PVP to the inorganic precursors and the NWs diameter, which was attributed to the difference of the crystallinity, porosity, and local micro-structures surrounding Ce^{3+}. Two decay time constants were observed for the PL of Ce^{3+}, one faster (1–3 ns) and one slower (10–20 ns), which were attributed to the hole-electron capture on the luminescent ions and isolated Ce ions, respectively. It is interesting to observe that for the shorter decay process, a maximum occurred as the concentration of Ce^{3+} varied in the range of 1–10 mol%.

R. Zheng · L. Xu · W. Qin · J. Chen · B. Dong · H. Song (✉)
State Key Laboratory on Integrated Optoelectronics, College of Electronic Science and Engineering, Jilin University, 2699 Qianjin Street, Changchun 130012, People's Republic of China
e-mail: hwsong2005@yahoo.com.cn

L. Zhang
Key Laboratory of Excited State Physics, Changchun Institute of Optics, Fine Mechanics and Physics, Chinese Academy of Sciences, 140 Ren-Min Street, Changchun 130022, People's Republic of China

Introduction

Since the discovery of carbon nanotubes, fabrication of one-dimensional nanomaterials has attracted wide attention because of their special physical and chemical properties and promising applications in optics [1–3], electronics [4–6], catalysts [7–10], and nanodevices [11–15]. So far, a number of preparation methods such as sputtering [16], vapor deposition [17], micro-emulsion [18], hydrothermal method [19], have been employed to synthesis one-dimensional nanostructures, However, these methods are either of costly or tedious in procedures. Therefore, the development of simple and cost-efficient methods to fabricate one-dimensional nanostructure in a large quantity is of great challenge. Electrospinning is such a method and has been widely used in the preparation of nanowires [1, 20] and nanotubes [1].

Many studies have proven that strontium aluminate ($SrAl_2O_4$) is an efficient host material with a wide band gap. When doped with rare earth ions or transition metal ions, it can generate broad band emissions [21]. It is well-known that $SrAl_2O_4$ belongs to the tridymite structure. All the AlO_4 tetrahedra are connected through the oxygen atoms to form the three-dimensional structure. On the basis of the above-mentioned advantages, a lot of researches have been conducted on the photoluminescence of rare earth-doped in the bulk or nanocrystalline $SrAl_2O_4$ [22–27].

At present, many studies about new luminescent materials have been focused on the synthesis and characterization of the short emission wavelengths material [28], because of their application in the imaging, lithography, and optical data recording. Trivalent cerium ions (Ce^{3+}) display a strong absorption in the UV region and a bright light emission [29], because the 5*d*–4*f* transition is

electric-dipole allowed [15, 27]. The decay time of the 5*d*–4*f* transition for Ce^{3+} is in the time scale of several ten nanoseconds, thus Ce^{3+}-doped phosphors are widely used as measurement of high-energy particle scintillation [2, 30–34].

As far as we know, there are only a few studies on the preparation and photoluminescence properties of $SrAl_2O_4:Ce^{3+}$ nanocrystalline [21, 33], especially, the electrospinning preparation of $SrAl_2O_4:Ce^{3+}$ NWs has not been reported. In this study, monoclinic $SrAl_2O_4:Ce^{3+}$ NWs were synthesized through electrospinning method for the first time, and their photoluminescence properties were investigated. FTIR, XPRD, SEM, photoluminescence spectra, and luminescent dynamics were employed to characterize the NWs.

Experimental procedures

Sample preparation

All chemicals were analytical grade and were used as received without further purification. Deionized water was used throughout. PVP-K90 ($M_w \approx 1300000$) was purchased from Aldrich. Ethanol (purity >99.7%), $Ce(NO_3)_3{\cdot}6H_2O$ (purity >99.99%), $Sr(NO_3)_2$ (purity >99.5%), $Al(NO_3)_3{\cdot}9H_2O$ (purity >99.0%), were all supplied by the Beijing Chemical Works.

The synthesis process of the samples is similar to one of our previous works [1]. First of all, the precursor solutions were obtained by the sol–gel technique. Then, the NWs were gained by electrospinning the above mentioned solutions. Next, the unwanted organic component was removed via thermal treatment. Typically, the mixture of $Sr(NO_3)_2$, $Al(NO_3)_3{\cdot}9H_2O$, and $Ce(NO_3)_3{\cdot}6H_2O$ in the molar ratio of 1: $(2-x)$: x ($x = 0.01$, 0.03, 0.05, 0.08, and 0.10) were dissolved in the 11 mL mixed solvent consisting of ethanol and deionized water with the volume ratio of 5:6. After stirring a few minutes, 1.4 g PVP was slowly added into the precursor solutions. The transparent solutions with suitable viscosity were obtained by further vigorous stirring for a few hours. The electrospinning device consists of three major components [1]: a high-voltage power supply, a spinneret (a plastic needle), and a collector plate (a grounded conductor). First of all, the electrospinning solution was added into 5 mL plastic syringe, and the high-voltage power wire was inserted from plastic syringe into the needle. Next, the stable Taylor cone was formed in the high-voltage electric field, when the electrospinning solutions emitted from the plastic needle. The NWs were collected on the collection plate with concurring evaporation of solvent to solidify the NWs. The electrospinning conditions are as follows: a collection distance of 15 cm between the spinneret tip and the collector; an applied steady voltage of 18 kV. After being dried for 12 h at room temperature under vacuum, the precursor NWs were first sintered in a tube furnace with a rise rate of 1 °C/min from room temperature and kept for 1 h at 600 °C. Then, the temperature was increased to 1000 °C at the same rate, and the samples were kept at 1000 °C for 2 h. Finally, the samples were naturally cooled to room temperature and the white mats were gained. Note that the whole sintering process was carried out under reducing atmosphere, which was produced by heating activated carbon. Thus, the annealing rate, temperature, and time are very important for holding the morphology of the NWs.

Characterization and measurements

The average diameters of the NWs were obtained by using the software named Nano-measurer to measure the diameters of more than 100 nanowires to get the average value. The X-ray diffraction (XRD) data were measured by a Rigaku D/max-rA X-ray diffractometer using a monochromatized Cu target radiation resource ($\lambda = 1.5045$ Å), with the scan ranging from 15° to 55° of 2θ and the scan speed of $2°min^{-1}$. The surface morphology of all the samples were performed with a JEOL JSM-7500F field emission scanning electron microscope (SEM) at an accelerating voltage of 15 kV with platinum sputtered on samples (20 mA, 60 s). The transmission electron microscope (TEM) images were recorded on a JEM-2010 transmission electron microscope under a working voltage of 200 kV equipped with EDX spectrometer. Fourier-transform infrared (FT–IR) spectra were obtained by the KBr pellet method in the range 400–4000 cm^{-1} using a Nexus 670 FT–IR spectrophotometer, the resolution of which is 1 cm^{-1}. Fluorescence and excitation spectra were recorded on a Hitachi F-4500 spectrophotometer equipped with a 150-W Xe arc lamp at room temperature. It is with a fixed band-pass of 0.2, 2.5 nm for excitation slit, 2.5 nm for emission slit and 700 V for PMT voltage to compare luminescent intensity in different samples. The resolution of the measurement is 2.5 nm. In order to measure the fluorescence dynamics of the samples, a FLS-920 singe-photon spectrometer using a nanosecond flash H_2-lamp was employed as excitation source. The excitation wavelength and emission wavelength were fixed at 318 and 366 nm, respectively.

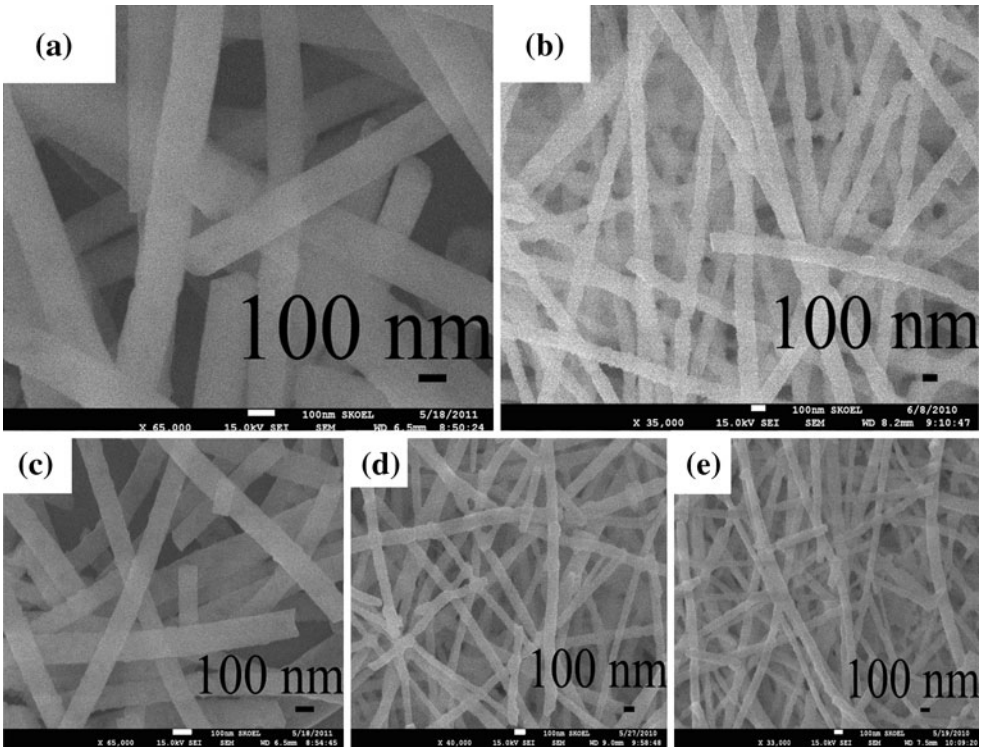

Fig. 1 SEM images of different $SrAl_2O_4$:Ce samples. **a** PVP/Inorganic = 4, **b** PVP/Inorganic = 5, **c** PVP/Inorganic = 5.7, **d** PVP/Inorganic = 6.8, **e** PVP/Inorganic = 7.3

Results and discussion

Structure and morphology of the one-dimensional NWs

Figure 1 shows the SEM images of $SrAl_2O_4:Ce^{3+}$ NWs with different weight ratios of PVP to inorganic (PVP/Inorganic). It can be observed that for all the samples, the products yielded NWs with high aspect-ratio, and they oriented randomly. When the ratio of PVP/Inorganic was in the range of 4.0–5.7, the NWs products were uniform and not adhesive to each other. When the ratio of PVP/Inorganic exceeded 5.7, the $SrAl_2O_4:Ce^{3+}$ NWs became a bit adhesive. Furthermore, by adjusting the PVP/Inorganic ratios, the diameters of the NWs were controlled in the range of 90–180 nm. As the ratio of PVP/Inorganic increased, actually the content of inorganic precursors decreased. During the calcination process, the NWs constricted with the removal of PVP. Obviously, more content of PVP lead to larger constriction. Table 1 lists the average diameters of different NWs products as well as the crystalline size, locations of excitation, and emission bands of Ce^{3+} determined in the following text. It is obvious that the larger the PVP/Inorganic ratio is, the smaller the average diameter of the NWs is. In order to further reveal the structure of NWs products, the TEM images of different NWs products are shown in Fig. 2. From the TEM image, it can be clearly seen that there are many pin holes in the NWs, which should originate from the volatilization of organic components in the annealing process. It should be noted that when the pin holes are too many, they can connect together, forming hollow structure. The formation of hollow structure prepared by electrospinning followed with annealing is affected by many factors, the two key ones are the annealing temperature and the ratio of Inorganic/PVP [1, 35]. They should both be controlled under an appropriate range, too low or too high will influence the formation of hollow structure. It was suggested some inorganic primary nanoparticles were firstly formed in the precursor fibers with the removing of PVP in the annealing, in both the outside and inner sites. At an appropriate

Table 1 A list of average grain sizes, diameters of NWs, locations of excitation, and emission bands of the products

PVP/Inorganic	Diameter (nm)	Grain size (nm)	Location of Excitation band (nm)	Location of emission band (nm)
4.0	180	36	321	366
5.0	120	18	321	364
5.7	106	26	318	368
6.8	100	29	319	366
7.3	90	33	322	371

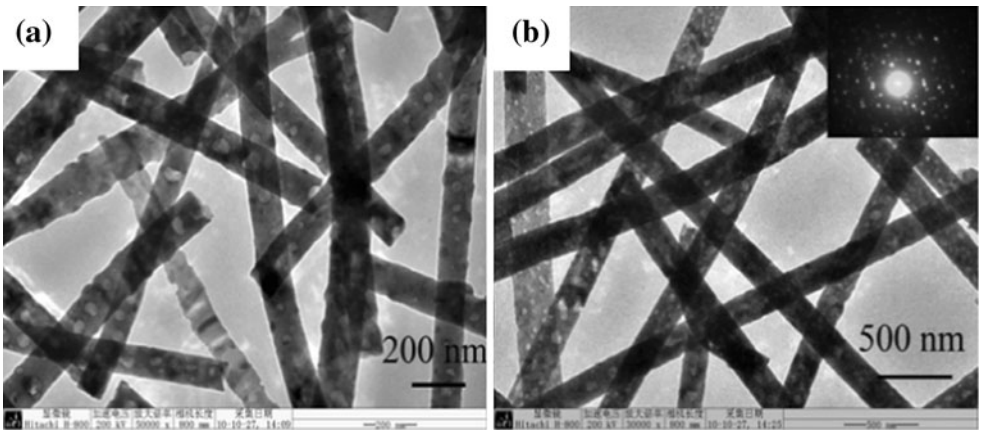

Fig. 2 TEM images of different samples. **a** PVP/Inorganic = 5.7, **b** PVP/Inorganic = 4, and SAED of $SrAl_2O_4$:Ce with PVP/Inorganic = 4

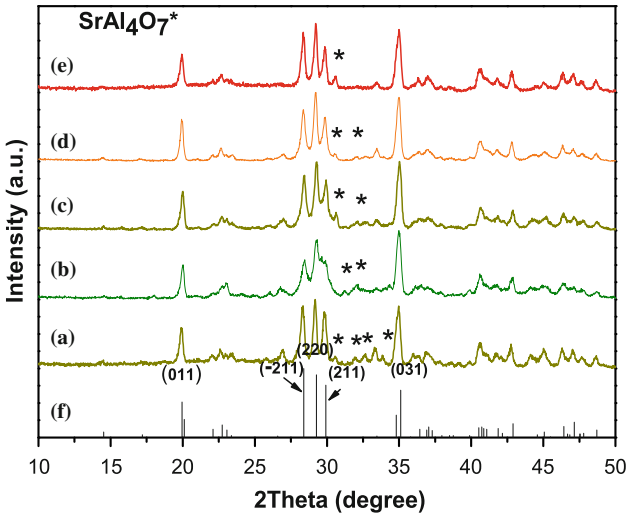

Fig. 3 XRD patterns of different $SrAl_2O_4$:Ce samples in contrast to JCPDS no.34-0379. **a** PVP/Inorganic = 4, **b** PVP/Inorganic = 5, **c** PVP/Inorganic = 5.7, **d** PVP/Inorganic = 6.8, **e** PVP/Inorganic = 7.3

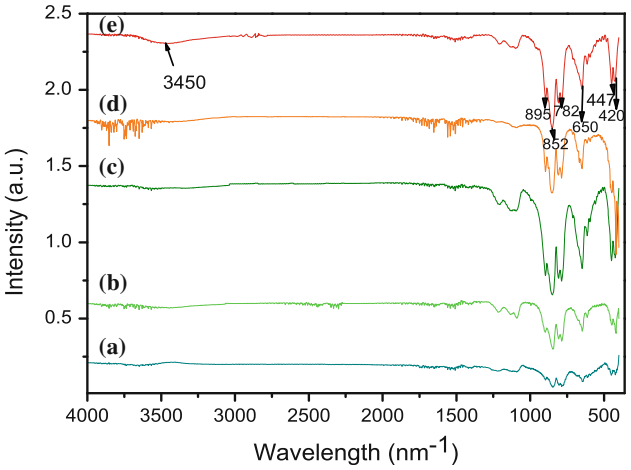

Fig. 4 FTIR spectra of different samples **a** PVP/Inorganic = 4, **b** PVP/Inorganic = 5, **c** PVP/Inorganic = 5.7, **d** PVP/Inorganic = 6.8, **e** PVP/Inorganic = 7.3

temperature, the reaction rate in the inner sites more quickly increased. In this case, the outside particles constricted, while the inner particles expanded due to large strain strength, leading to the formation of hollow structure. The inset in Fig. 2b displays the SAED patterns of $SrAl_2O_4$:Ce NWs with ratio of PVP/Inorganic = 4, which reveals the polycrystalline nature of the sample.

Figure 3 depicted the XRD patterns of the $SrAl_2O_4$:Ce NWs. It can be seen that all the samples are well crystalline, and most of the peaks could be readily indexed to the monoclinic monazite $SrAl_2O_4$ phase (JCPDS no. 34-0379). Some main patterns have been labeled in contrast to the standard card. The XRD peaks for all the samples are sharp and intense, which indicates the high crystallinity of the samples. Besides, a little bit of the impure phase, monoclinic $SrAl_4O_7$ (JCPDS no. 70-1479) can be found in the NWs products, as labeled by star in the figure. It looks like that the products prepared with smaller ratio of PVP/Inorganic leads to more impure phase. This implies that the improved content of PVP favor the formation of $SrAl_2O_4$ phase and can prevent the formation of $SrAl_4O_7$ impurity phase to a certain extent. We suggest that the existent of PVP made the precursor nanowires before annealing have reduction atmosphere, preventing $SrAl_2O_4$ from oxidation. As is well-known, the average nanocrystalline size of the nanoparticles can be calculated by the Debye–Scherrer formula on the (220) diffraction peaks [36],

$$d = \frac{k\lambda}{\mathrm{B}\cos\theta}, \tag{1}$$

where d is the average size of the grain, K is a constant (0.89), λ is the wavelength of the X-ray radiation (Cu Ka = 0.1541 nm), B is the full width at half-maximum (FWHM), and θ is the diffraction angle. Based on Eq. 1 and the width of the XRD patterns, the average crystalline

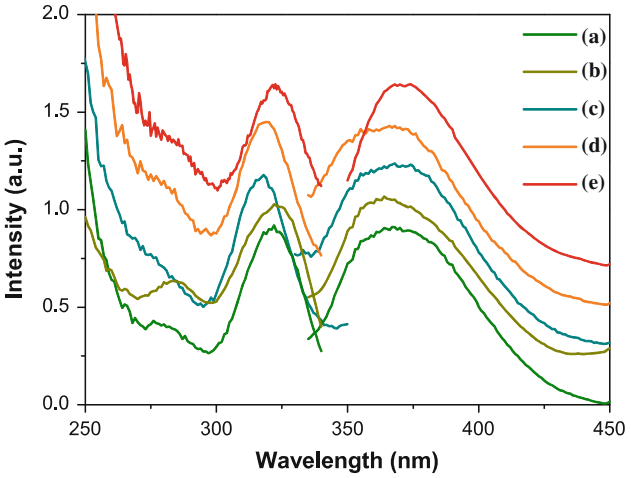

Fig. 5 Room temperature excitation and emission spectra of different $SrAl_2O_4$:Ce (3%) samples. **a** PVP/Inorganic = 4, **b** PVP/Inorganic = 5, **c** PVP/Inorganic = 5.7, **d** PVP/Inorganic = 6.8, **e** PVP/Inorganic = 7.3

sizes of different samples are determined, as listed in Table 1. It is obvious that the average crystalline sizes of the NWs are much smaller than their real diameters. In addition, the variation of average crystalline size of the NWs products is independent of the ratio of PVP/Inorganic.

The FTIR spectra of the samples were shown in Fig. 4. All the indentified bands have been marked in the figure. According to the literature [37], the vibration modes of PVP occur in the range of 1200–3500 cm^{-1}. From the figure, we can see clearly that the bands corresponding to organic components completely disappeared, implying that the starting PVP completely dissolved owing to high annealing temperature. The bands between 400 and 1000 cm^{-1} can be all assigned to the vibrations of $SrAl_2O_4$. The symmetric bending of O–Al–O appears as a double at 447 and 420 cm^{-1} [26]. The antisymmetric stretching bands ranging of 550–650 cm^{-1} are attributed to the Sr–O vibrations [37, 38]. The band located at 852 cm^{-1} is Sr–O. The bands positioned at 786 and 895 cm^{-1} originate from the aluminates groups(AlO_4) [39]. Besides, two additional bands at 1125 and 1250 cm^{-1} appear which both can be assigned to the C–O vibrations. At present, we can not give a proper explanation on how the C–O vibrations are involved in the samples. The bands locating at 3450 cm^{-1} is the symmetric vibration of –OH groups.

Photoluminescence and dynamics

Excitation and emission spectra

Figure 5 reveals the room-temperature excitation and emission spectra of the $SrAl_2O_4$:Ce (3%) prepared at

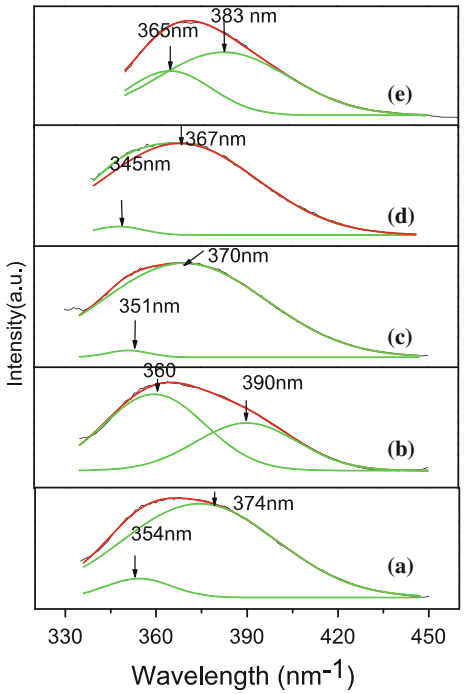

Fig. 6 Dissolved emission spectra of the $SrAl_2O_4$:Ce (3%) products

different conditions. In the left part, the excitation peaks consist of two bands, located at ~ 280 and ~ 320 nm [21], respectively. The bands at 320 nm are much stronger. The two excitation bands are associated with the allowed $4f$–$5d$ transitions from the ground state $^2F_{5/2}$ to different crystal-field components of the excited $5d$ state. In the right part, emission bands ranging of 330–450 nm [21] appear, which can be dissolved into two peaks, originating from the transitions from the lowest $5d$ excited state to the spin–orbit components (D^2) of the doublet ground state, $^2F_{5/2}$, $^2F_{7/2}$ [39]. From the figure, we can see that the positions of excitation and emission bands shift a little with changing the weight ratio of PVP/Inorganic. The position of the emission band varies from 364 to 371 nm, while the main excitation band changes from 317 to 322 nm, as shown in Table 1. The reason may be related to uncontrollable electrospinning conditions, such as air and wetness, which leads to the difference of the crystallinity, porosity, and micro-dimensions of the products, thus further influencing the crystal field surrounding Ce^{3+}.

In order to further understand the photoluminescent properties of the NWs products, the emission spectra of different samples are dissolved by two-Gaussian functions, as shown in Fig. 6. It can be seen that the locations and relative contributions of the two bands, vary largely but irregularly with the products. The energy separations between the two bands, were determined to be 1510, 2000, 1463, 1738, and 1287 cm^{-1}, respectively, for the NW products with ratios of PVP/Inorganic = 4, 5, 5.7, 6.8, and

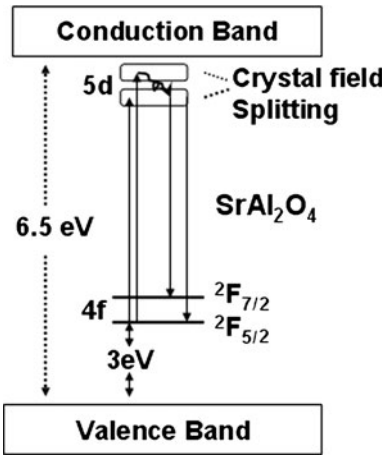

Fig. 7 Schematic diagram of band gap, energy levels, and photoluminescence of $SrAl_2O_4$:Ce

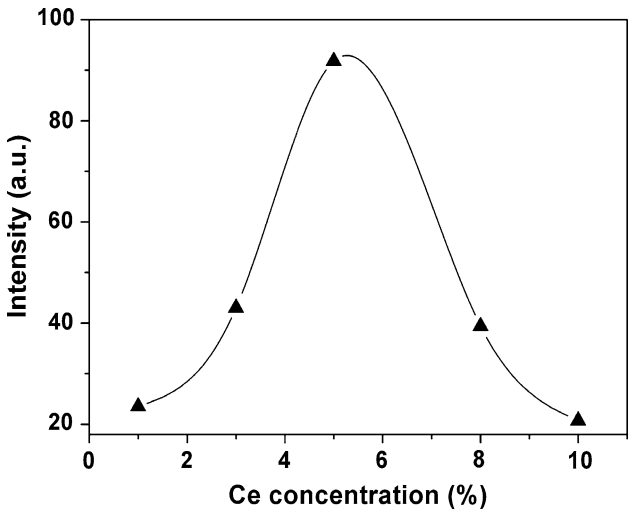

Fig. 8 Emission intensity as a function of doping concentration of Ce (All the samples were prepared with PVP/Inorganic = 4)

7.3. This energy separation should correspond to the energy gap of $^2F_{2/5}$ and $^2F_{2/7}$. Figure 7 draws the schematic diagram of band gap, energy levels, and photoluminescence of $SrAl_2O_4$:Ce [33].

Figure 8 shows emission intensity of Ce^{3+} as a function of Ce-doped concentration. It can be seen that the emission intensity increases with the increase of the Ce concentration in the range of 1–5 mol%. Moreover, the strongest intensity appears when the Ce concentration approach to 5 mol%. While the Ce concentration surpass 5 mol%, the intensity gradually decreases with the increasing Ce concentration. In low Ce concentration range, the number of the luminescence centers becomes more with the increase of the doping concentration, which results in fluorescence enhancement. After the doping concentration exceed a certain value, the luminescent centers continue to increase and the distance among the luminescent centers become close, which results in the energy transfer between any two neighboring luminescent centers and leads to concentration quenching [40].

Luminescent dynamics

Figure 9 shows comparative decay curves of $SrAl_2O_4:Ce^{3+}$ phosphors with different PVP/Inorganic ratios, 4, 5, and 5.7, which correspond to the average diameter of 180, 120, and 106 nm, respectively. All the curves can be well-fitted using a double-exponential function [41],

$$I = I_1 * \exp(-t/\tau_1) + I_2 * \exp(-t/\tau_2), \quad (2)$$

where τ_1 and τ_2 correspond to shorter and longer lifetime constants for the 4*f*–5*d* transitions of Ce^{3+}, respectively, I_1 and I_2 represent their relative contributions ($I_1 + I_2 = 1$). For the 180, 120, and 106 nm samples, τ_1 were determined to be 5, 2.4, and 1.6 ns, respectively, τ_2 to be 26, 16, and 17.8 ns, respectively, I_1 to be 0.56, 0.80, and 0.66, and I_2 to be 0.44, 0.20, and 0.34, respectively. It is suggested that the faster component arises from the hole-electron capture on the luminescent ions [Ce^{4+}+e → (Ce^{3+})*] and the slower component arises from isolated Ce^{3+} ions [30]. It can be clearly seen that the lifetime becomes shorter with the decreased diameter of the NWs. Thus, we can conclude that the size of NWs plays a vital role in the variation of lifetime. In the formation of $SrAl_2O_4:Ce^{3+}$ NWs, the removal of PVP leads to the formation of defect states. The more the PVP content is, the more the defect states are. These defects act as quenching centers, leading to the increase of non-radiative relaxation rate and the decrease of lifetime. At present, we can not conclude that these defect states distribute only on the surface of $SrAl_2O_4:Ce^{3+}$ NWs. Because of the large NWs diameters (90–180 nm), the surface to volume ratio of the $SrAl_2O_4:Ce^{3+}$ NWs is small all the time, so the surface effect should not be obvious.

The decay curves of $SrAl_2O_4:Ce^{3+}$ phosphors with different Ce concentrations were also measured. All the curves can be well-fitted using a double-exponential function, and the obtained lifetimes and their relative contributions are shown in Table 2. It can be seen that the shorter lifetime constant first increases with the increase of Ce and approaches to a maximum value at 5 mol%. Then it decreases obviously as the concentration of Ce increase continuously. The increase of Ce^{3+} lifetime could be attributed to radiative trapping, in which a photon once emitted by a luminescence center is absorbed by another center of the same kind. As photons "trapped" in this way are usually emitted again, the basic consequence of radiation trapping is a prolongation of the emission decay time [42]. The other possible reason, with the increase of Ce

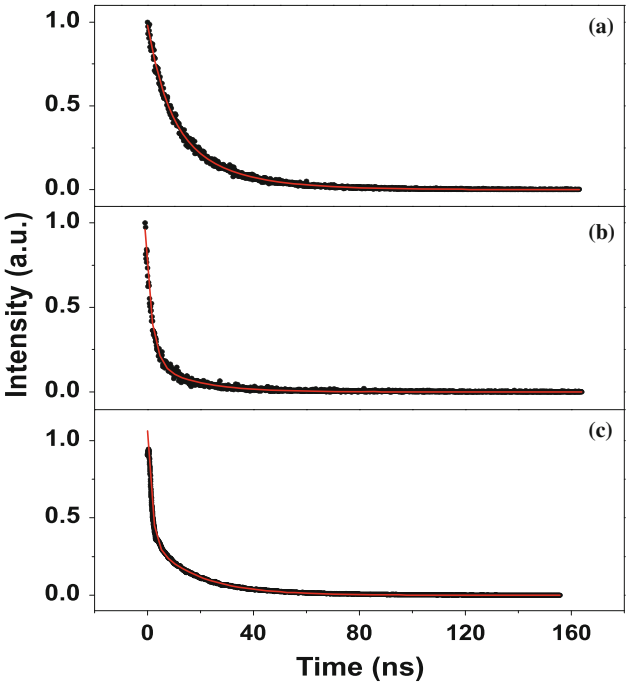

Fig. 9 The decay curves of $SrAl_2O_4:Ce^{3+}$ phosphor among different PVP/Inorganic ($\lambda_{em} = 366$ nm) **a** PVP/Inorganic = 4, **b** PVP/Inorganic = 5, **c** PVP/Inorganic = 5.7

Table 2 Bi-exponential decay constants and their relative contributions of the samples with different doped Ce concentrations

Doping concentration Ce^{3+} (mol%)	I_1	I_2	τ_1 (ns)	τ_2 (ns)
1	0.66	0.34	1.1	16.6
3	0.74	0.26	1.4	16.0
5	0.52	0.48	2.6	16.6
8	0.72	0.28	1.5	18.0
10	0.76	0.24	1.0	11.0

concentration, the internal defects reduce, which leads to the decrease of the non-radiative transition rate and increase of the lifetime [30]. When the Ce concentration reaches a certain value, the energy transfer between Ce^{3+} ions happens considerably, leading the non-radiative transition rate to increase and concentration quenching, so the lifetimes become shorter. The longer lifetime constant has only a little variation when the Ce concentration is less than 8%. However, it decreases quickly when the concentration approaches to 10% due to concentration quenching.

Conclusions

We synthesized monoclinic $SrAl_2O_4:Ce^{3+}$ NWs with diameters of 90–180 nm by the electrospinning method. They are characterized by techniques such as SEM, TEM, XRD, FTIR spectra, PL spectra, and dynamics. The results demonstrate that the ratio of PVP/Inorganic influences the structure and photoluminescent properties largely. The average diameter of the NWs gradually decreases with the increase of PVP/Inorganic due to the larger constriction of NWs with the removal of PVP. This also leads to the formation of more defect states, which induce larger non-radiative relaxation rates and decreased lifetime constants for the PL of Ce^{3+}. In the $SrAl_2O_4:Ce^{3+}$ NWs, the excitation and emission bands vary with samples irregularly. The PL of Ce^{3+} exist two decay time constants, including one faster (1–3 ns) and one slower (10–20 ns), which are attributed to the hole-electron capture on the luminescent ions and isolated Ce ions, respectively. It is also interesting to observe that for the shorter decay process, the decay time constant of Ce^{3+} first increases with the increase of Ce^{3+}, and approaches to the maximum at 5 mol% Ce^{3+}, then decreases with the increase of Ce^{3+}.

Acknowledgements The authors are thankful for the financial support of Distinguished Young Scholars of China (Grant no. 60925018), the National Natural Science Foundation of China (Grant nos. 50772042, 51002062, and 20971051).

References

1. Xu L, Song HW, Dong B, Wang Y, Bai X, Wang GL, Liu Q (2009) J Phys Chem C 113:9609
2. Suryamas AB, Munir MM, Iskandar F, Okuyama K (2009) J Appl Phys 105:064311
3. Cacciotti I, Bianco A, Pezzotti G, Gusmano G (2011) Chem Eng J 166:751
4. Wu H, Hu LB, Rowell MW, Kong DS, Cha JJ, McDonough JR, Zhu J, Yang Y, McGehee MD, Cui Y (2010) Nano Lett 10:4242
5. Tse KY, Zhang LZ, Baker SE, Nichols BM, West R, Hamers RJ (2007) Chem Mater 19:5734
6. Samitsu S, Shimomura T, Heike S, Hashizume T, Ito K (2008) Macromolecules 41:8000
7. Liu ZY, Sun DD, Guo P, James OL (2007) Nano Lett 74:1081
8. Yang DJ, Liu HW, Zheng ZF, Yuan Y, Zhao JC, Waclawik ER, Ke XB, Ke HY (2009) J Am Chem Soc 131:17885
9. Wang FC, Liu CH, Liu CW, Chao JW, Lin CH (2009) J Phys Chem C 113:13832
10. Dai YQ, Liu WY, Formo E, Sun YM, Xia YN (2011) Polym Adv Technol 22:326
11. Xu L, Dong B, Wang Y, Bai X, Liu Q, Song HW (2010) Sens Actuators B Chem 147:531
12. Zong SZ, Cao Y, Zhou YM, Ju HX (2007) Biosens Bioelectron 22:1776
13. Jiang ZW, Guo Z, Sun B, Jia Y, Li MQ, Liu JH (2010) Sens Actuators B Chem 145:667
14. Zhang ZY, Li XH, Wang CH, Wei LM, Liu YC, Shao CG (2009) J Phys Chem C 113:19397
15. Yu JH, Chioi GM (2001) Sens Actuators B-Chem 75:56
16. Korotcov AV, Huang YS, Tsai DS, Tiong KK (2006) Thin Solid Films 503:96
17. Wei DP, Ma Y, Pan HY, Chen Q (2008) J Phys Chem C 112:8594

18. Yu YJ, Ouyang C, Gao Y, Si ZH, Chen W, Wang ZQ, Xue G (2005) J Polym Sci Part A Polym Chem 43:6105
19. Vasco E, Magrez A, Forro L, Setter N (2005) J Phys Chem B 109:14331
20. Cacciotti I, Bianco A, Pezzotti G, Gusmano G (2011) Mater Chem Phys 126:532
21. Fu ZL, Zhou SH, Zhang SY (2005) J Phys Chem B 109:14396
22. Jung KY, Lee HW, Jung HY (2006) Chem Mater 18:2249
23. Poort SHM, Blokpoel WP, Blasse G (1995) Chem Mater 7:1547
24. Clabau F, Rocquefelte X, Jobic S, Deniard P, Whangbo MH, Garcia A, Mercier TL (2005) Chem Mater 17:3904
25. Liu Y, Xu CN (2003) J Phys Chem B 107:3991
26. Chen JT, Gu F, Li CZ (2008) Cryst Growth Des 8:3175
27. Chen XY, Ma C, Li XX, Shi CW, Li XL, Lu DR (2009) J Phys Chem C 113:2685
28. Lai H, Bao A, Yang YM, Tao YC, Yang H, Zhang Y, Han LL (2008) J Phys Chem C 112:282
29. Wang HY, Wang Y, Yang Y, Li X, Wang Ce (2009) Mater Res Bull 44:408
30. Saha S, Chowdhury PS, Patra A (2005) J Phys Chem B 109:2699
31. Kumar V, Pitale SS, Mishra V, Nagpure IM, Biggs MM, Ntwaeaborwa OM, Swart HC (2010) J Alloy Comp 492:L8
32. Nyman M, Shea-Rohwer LE, Martin JE, Provencio P (2009) Chem Mater 21:1536
33. Zhang HW, Yamada H, Terasaki N (2007) Appl Phys Lett 91:081905
34. Im WB, Fellows NN, DenBaars SP, Seshadri R, Kim Y (2009) Chem Mater 21:2957
35. Song HW, Yu HQ, Pan GH, Bai X, Dong B, Zhang XT, Hark SK (2008) Chem Mater 20:4762
36. Sapra S, Prakash A, Ghangrekar A, Periasamy N, Sarma DD (2005) J Phys Chem B 109:1663
37. Cheng YL, Zhao Y, Zhang YF, Cao XQ (2010) J Colloid Interface Sci 344:321
38. Lavat AE, Grasselli MC, Lovecchio EG (2010) Ceram Int 36:15
39. Tarte P (1967) Spectrochim Acta A 237:2127
40. Sole JG, Bausa LE, Jaque D (2005) John Wiley & Sons Ltd., New York, p 200
41. Yu LX, Song HW, Liu ZX, Yang LM, Lu SZ, Zheng ZH (2005) J Phys Chem B 109:11450
42. Drozdowski W, Wojtowicz AJ (2002) Nucl Instrum Meth A 408:412